An Hα Impression of Lyα Galaxies at $z \simeq 6$ with Deep JWST/NIRCam Imaging

Yuanhang Ning[1] , Zheng Cai[1] , Linhua Jiang[2,3] , Xiaojing Lin[1] , Shuqi Fu[2,3] , and Daniele Spinoso[1]

[1] Department of Astronomy, Tsinghua University, Beijing 100084, People's Republic of China; ningyhphy@mail.tsinghua.edu.cn, zcai@mail.tsinghua.edu.cn

[2] Kavli Institute for Astronomy and Astrophysics, Peking University, Beijing 100871, People's Republic of China

[3] Department of Astronomy, School of Physics, Peking University, Beijing 100871, People's Republic of China

Abstract

We present a study of seven spectroscopically confirmed (Lyα-emitting) galaxies at redshift $z \simeq 6$ using the JWST/NIRCam imaging data. These galaxies, with a wide range of Lyα luminosities, were recently observed in a series of NIRCam broad and medium bands. We constrain the rest-frame UV/optical continua and measure the Hα line emission of the galaxies using the combination of JWST/NIRCam and archival HST/WFC3 infrared photometry. We further estimate the escape fractions of their Lyα photons ($f_{\rm esc}^{\rm Ly\alpha}$) and the production efficiency of ionizing photons ($\xi_{\rm ion}$). Among the sample, six out of seven galaxies have Lyα escape fractions of $\lesssim 10\%$, which might be the status for most of the star-forming galaxies at $z \simeq 6$. One UV-faint Lyα galaxy with an extremely blue UV slope has a large value of $f_{\rm esc}^{\rm Ly\alpha}$ reaching $\simeq 50\%$. These galaxies have a broad range of $\xi_{\rm ion}$ over $\log_{10} \xi_{\rm ion,0}$ (Hz erg^{-1}) ~ 25.0–26.5. We find that UV-fainter galaxies with bluer UV-continuum slopes likely have higher escape fractions of Lyα photons. We also find that galaxies with higher Lyα line emission tend to produce ionizing photons more efficiently. The most Lyα-luminous galaxy in the sample has a very high $\xi_{\rm ion,0}$ of $\log_{10} \xi_{\rm ion,0}$ (Hz erg^{-1}) > 26. Our results support the scenario that Lyα galaxies may have served as an important contributor to cosmic reionization. Blue and bright Lyα galaxies are excellent targets for JWST follow-up spectroscopic observations.

Unified Astronomy Thesaurus concepts: High-redshift galaxies (734); Lyman-alpha galaxies (978); Galaxy properties (615); Reionization (1383); James Webb Space Telescope (2291)

1. Introduction

The James Webb Space Telescope (JWST; Gardner et al. 2006) has begun to explore the very distant universe, allowing us to gain deep insight into the high-redshift (high-z) objects at the epoch of reionization (EoR). The major sources of reionization are presumably star-forming (SF) galaxies (e.g., Robertson et al. 2015; Finkelstein et al. 2019; Yung et al. 2020a). This viewpoint has been conclusively demonstrated by Jiang et al. (2022). As a population of SF galaxies, Lyα-emitting galaxies are generally low mass with low metallicity and dust content (e.g., Hao et al. 2018; Arrabal Haro et al. 2020; Santos et al. 2020). They should play a nonnegligible role in driving reionization because the processes responsible for the emission of Lyα and Lyman-continuum (LyC) photons relate to each other (e.g., Dijkstra 2014; Verhamme et al. 2015; de Barros et al. 2016; Dijkstra et al. 2016) while the Lyα escape fraction ($f_{\rm esc}^{\rm Ly\alpha}$) generally exceeds LyC escape fraction ($f_{\rm esc}^{\rm LyC}$; e.g., Izotov et al. 2016; Leitherer et al. 2016; Shapley et al. 2016; Verhamme et al. 2017; Izotov et al. 2020; Flury et al. 2022).

Large ground-based telescopes and the Hubble Space Telescope (HST) helped us find a large number of Lyα-emitting galaxies with redshift reaching $z \gtrsim 6$–7, corresponding to the end of EoR. Most of them are Lyα emitters (LAEs) selected by the narrowband (Lyα) technique (e.g., Kashikawa et al. 2006; Hu et al. 2010; Kashikawa et al. 2011; Shibuya et al. 2018; Taylor et al. 2021). The rest of them are Lyman-break galaxies (LBGs) selected by the dropout technique and

identified by Lyα lines (e.g., Steidel et al. 1996; Jones et al. 2012; Inami et al. 2017; Pentericci et al. 2018). The LAEs and LBGs (with Lyα lines) are probably indistinguishable in terms of their intrinsic properties such as age, stellar mass, and star formation rate (SFR; e.g., Dayal & Ferrara 2012; Jiang et al. 2016; de La Vieuville et al. 2020). We thus call both of them Lyα galaxies in the following text.

To understand how SF galaxies contribute to the ionizing photon budget, their rest-frame optical properties (continua and line emission) are necessary to constrain. However, this task was difficult to execute before the JWST era, especially for $z \simeq 6$ galaxies. For example, due to a lack of near-/mid-infrared (IR) bands, it is challenging to break the degeneracy between prominent nebular emission from young galaxies and strong Balmer breaks from old galaxies (e.g., Schaerer & de Barros 2009; Jiang et al. 2016). On the other hand, even if the galaxies are spectroscopically confirmed (by Lyα line for instance) at $z \simeq 6$, the optical emission lines (mainly [O III] +Hβ and Hα+[N II]) simultaneously boost the IRAC1 and IRAC2 channels of Spitzer Space Telescope (e.g., Faisst et al. 2016; Harikane et al. 2018; Stefanon et al. 2021), leaving lines and continua coupled together. Such problems are being solved in the current JWST era.

To build a large and homogeneous sample of high-z galaxies, we have carried out the Magellan M2FS spectroscopic survey to identify LAEs and LBGs at $z \simeq 6$ (Jiang et al. 2017; Ning et al. 2020, 2022; S. Fu et al. 2023, in preparation). A fraction of them will be covered by the upcoming JWST imaging survey, such as COSMOS-Webb (GO 1727; Kartaltepe et al. 2021; Casey et al. 2022) and PRIMER (GO 1837; Dunlop et al. 2021). Multiple IR bands can reveal their individual properties in detail. Recently, one of our identified LBGs has been covered by parallel JWST/NIRCam imaging of

Table 1
Basic Information and Photometry of the Lyα Galaxy Sample at $z \simeq 6$

ID	SC-1	SC-2	SC-3	SC-4	SC-5	SC-6	SC-7
R.A. (J2000.0)	02:17:43.25	02:17:48.31	02:17:25.12	03:32:28.19	03:32:36.47	03:32:38.28	03:32:39.06
Decl. (J2000.0)	−05:06:47.5	−05:10:31.7	−05:11:35.0	−27:48:18.7	−27:46:41.4	−27:46:17.2	−27:45:38.7
Redshift $z_{\mathrm{Ly}\alpha}$	6.087	5.810	6.297	5.939	5.938	6.108	5.916
CANDELS field	(UDS)[a]	UDS	UDS	GOODS-S	GOODS-S	GOODS-S	GOODS-S
JWST ObsID	PRIMER-o022	PRIMER-o022	PRIMER-o014	UDF-MB	UDF-MB	UDF-MB	UDF-MB
F090W (mag)	26.58 ± 0.07	26.02 ± 0.04	⋯	⋯	⋯	⋯	⋯
F105W (mag)	⋯	⋯	⋯	26.15 ± 0.06	25.76 ± 0.03	26.31 ± 0.03	27.64 ± 0.07
F115W (mag)	26.56 ± 0.07	25.56 ± 0.03	⋯	⋯	⋯	⋯	⋯
F125W (mag)	⋯	25.56 ± 0.09	26.39 ± 0.17	26.15 ± 0.07	25.70 ± 0.02	26.35 ± 0.02	27.73 ± 0.06
F150W (mag)	26.76 ± 0.08	25.30 ± 0.02	⋯	⋯	⋯	⋯	⋯
F160W (mag)	⋯	25.49 ± 0.10	26.51 ± 0.16	26.04 ± 0.07	25.70 ± 0.02	26.32 ± 0.02	28.06 ± 0.08
F182M (mag)	⋯	⋯	⋯	26.32 ± 0.01	26.20 ± 0.01	26.32 ± 0.01	27.46 ± 0.02
F210M (mag)	⋯	⋯	⋯	26.21 ± 0.01	26.07 ± 0.01	26.28 ± 0.01	27.15 ± 0.02
F200W (mag)	26.57 ± 0.07	25.22 ± 0.02	⋯	⋯	⋯	⋯	⋯
F277W (mag)	26.20 ± 0.04	24.80 ± 0.01	25.97 ± 0.03	⋯	⋯	⋯	⋯
F356W (mag)	25.06 ± 0.01	24.57 ± 0.01	25.21 ± 0.01	⋯	⋯	⋯	⋯
F410M (mag)	25.93 ± 0.07	24.66 ± 0.02	26.26 ± 0.09	⋯	⋯	⋯	⋯
F444W (mag)	24.73 ± 0.02	24.53 ± 0.02	25.67 ± 0.04	⋯	⋯	⋯	⋯
F430M (mag)	⋯	⋯	⋯	26.42 ± 0.09	26.03 ± 0.06	26.27 ± 0.08	27.67 ± 0.34
F460M (mag)	⋯	⋯	⋯	25.06 ± 0.03	24.56 ± 0.02	25.51 ± 0.04	25.80 ± 0.07
F480M (mag)	⋯	⋯	⋯	26.31 ± 0.09	25.92 ± 0.06	25.79 ± 0.05	>27.62[b]

Notes.
[a] The parentheses indicate that SC-1 is located close to the CANDELS UDS imaging region.
[b] This value corresponds to a 3σ upper limit.

PRIMER MIRI observations. In this work, we compare it with spectroscopically confirmed galaxies at $z \simeq 6$ from previous literature (Pentericci et al. 2018) as a pilot investigation into the Hα properties of luminous Lyα galaxies.

This paper is organized as follows. In Section 2, we briefly present the sample of Lyα galaxies, JWST/NIRCam imaging observations, data reduction, and photometry. In Section 3, we give the measurement results of the Lyα-, ultraviolet- (UV-), and Hα-related properties of the galaxy sample. We discuss their Lyα escape fractions and ionizing photon production efficiencies in Section 4. We summarize this work in Section 5. Throughout the paper, we use a standard flat cosmology with $H_0 = 70 \ \mathrm{km \ s^{-1} \ Mpc^{-1}}$, $\Omega_\mathrm{m} = 0.3$, and $\Omega_\Lambda = 0.7$. All magnitudes refer to the AB system (Oke 1974).

2. Sample and Data

In this section, we describe our sample of Lyα galaxies at $z \simeq 6$, JWST/NIRCam imaging observations, data reduction, and photometry. We summarize the sample information in Table 1.

2.1. Sample of Lyα Galaxies at z ≃ 6

The sample includes seven spectroscopically confirmed galaxies at $z \simeq 6$. The first one (SC-1) is confirmed at redshift $z = 6.087$ with a strong Lyα line by our spectroscopic survey (see the upper panel of Figure 1; S. Fu et al. 2023, in preparation). In this survey, we carried out spectroscopic observations using the fiber-fed, multiobject spectrograph Michigan/Magellan Fiber System (M2FS; Mateo et al. 2012) on the 6.5 m Magellan Clay telescope. The science goal is to build a large and homogeneous sample of high-z galaxies (see Jiang et al. 2017 for an overview of the program), including LAEs at $z \approx 5.7$ and 6.6 (Ning et al. 2020, 2022) and LBGs at
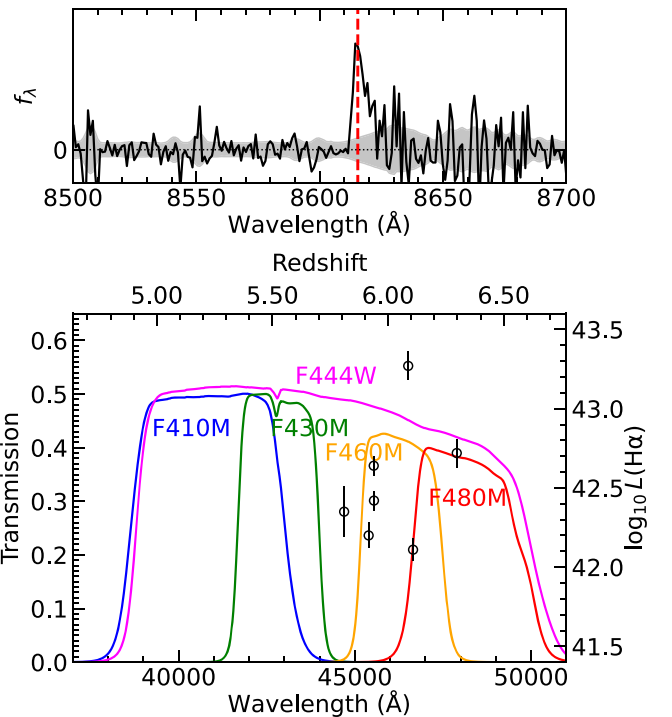

Figure 1. Upper panel: the spectrum of the Lyα galaxy (SC-1 with $z_{\mathrm{Ly}\alpha} = 6.087$) confirmed by our Magellan M2FS spectroscopic survey. The vertical dashed line marks the observed Lyα wavelength. The shaded region represents the $\pm 1\sigma$ noise level. Lower panel: the redshift–Hα luminosity distribution of the sample in this work and the transmission curves of the five JWST/NIRCam filters. The highest data point corresponds to our confirmed galaxy (SC-1) shown in the upper panel.

$5.5 < z < 6.8$ (S. Fu et al. 2023, in preparation). These high-z galaxies are located in famous fields, including the Subaru XMM-Newton Deep Survey (SXDS), the Extended Chandra

Deep Field-South (ECDFS), A370, COSMOS, and SSA22. The total sky area is around 2 deg^2. SC-1 has an estimated Lyα equivalent width (EW) of EW$_0$ (Lyα) $\gtrsim$ 100 Å. It is thus one of the largest-EW$_0$ (Lyα) LBGs in a wide area covered by our spectroscopic survey.

The other six sources (SC-2–7) are from previous work (Pentericci et al. 2018, hereafter P18). They used VLT/FORS2 to conduct the CANDELSz7 survey, an ESO Large Program, to spectroscopically confirm SF galaxies at $z \gtrsim 6$ in three HST CANDELS Legacy fields (GOODS-South, UDS, and COSMOS). SC-2 and SC-3 are located in the CANDELS UDS field, while SC-4–7 is located in the CANDELS GOODS-South (GOODS-S) field. Among them, SC-2 was detected with no emission line and a continuum discontinuity which is interpreted as a Lyα break (see P18). Due to the limited sensitivity of instruments and depth of observations, we treat this source as a Lyα galaxy with an upper limit of EW$_0$ (Lyα) from P18. Figure 1 shows the redshift distribution of the sample in the lower panel.

2.2. Imaging Data

The three sources SC-1–3 in/around the CANDELS UDS field are covered by the JWST Cycle-1 program (GO 1837), Public Release IMaging for Extragalactic Research (PRIMER; Dunlop et al. 2021). The PRIMER survey pays attention to the two key equatorial HST CANDELS Fields (COSMOS and UDS) by delivering 10-band NIRCam+MIRI imaging observations. It owns the parallel NIRCam imaging in eight bands, including F090W, F115W, F150W, and F200W in the short wavelength (SW), and F277W, F356W, F444W, and F410M in the long wavelength (LW). Note that the F410M − F444W color is a good indication of the Hα emission of the SF galaxies at $z \sim 5$–6.6. SC-1–3 have been imaged by PRIMER #14 and #22 observations with individual exposure lengths of $\sim$1.9 hr in the SW bands and $\sim$0.5 hr in the LW bands.

The other four sources, SC-4–7, are covered by the JWST Cycle-1 program (GO 1963), the UDF medium-band survey (UDF-MB; Williams et al. 2021). The UDF-MB survey images the (Hubble) Ultra Deep Field (UDF) with a single NIRCam pointing (field of view $\sim$2 × 2$'$2 × 2$'$2) in a series of medium bands including F182M, F210M, F430M, F460M, and F480M (NIRISS F430M and F480M in parallel). The total integration time reaches $\sim$7.8 hr for F182M, F210M, and F480M and $\sim$3.9 hr for F430M and F460M. In Figure 1, we plot the transmission curves of the five JWST/NIRCam LW filters to compare and illustrate the Hα locations of the galaxies in the observed wavelength frame.

Except for SC-1 and 2, other sources are not covered by enough JWST SW bands, especially SC-3, which is located in the gap region of NIRCam SW imaging. We thus utilize the archival HST/WFC3 (Wide Field Camera 3) near-IR imaging data from the CANDELS program (Grogin et al. 2011; Koekemoer et al. 2011; Guo et al. 2013; Galametz et al. 2013). We download the data products provided by the High Level Science Products.[4] SC-2 and SC-3 have HST/WFC3 F125W and F160W observations while SC-1 is a little bit outside the CANDELS UDS region. SC-4–7 in the CANDELS GOODS-S region have HST/WFC3 observations in three near-IR bands (F105W, F125W, and F160W).

2.3. Data Reduction and Photometry

We reduced the NIRCam imaging data with the standard JWST pipeline[5] (v1.7.2) up to stage 2 using the reference files "jwst_0999.pmap" for PRIMER and "jwst_1008.pmap" for UDF-MB. Then we use the `Grizli`[6] reduction pipeline to process the output images. `Grizli` mitigates 1/f noises and masks the "snowball" artifacts from cosmic rays (Rigby et al. 2022). It further converts the world coordinate system (WCS) information in the headers to the SIP format for each exposure so that images can be drizzled and combined with Astro-drizzle.[7] For the SW and LW images, the WCS of final mosaics are registered based on the catalogs of DESI Legacy Imaging Surveys Data Release 9 and the pixel scale was resampled to $0''\!.03$ with pixfrac = 0.8. We also subtract an additional background on the final mosaics. Figure 2(a) shows the thumbnail images of the sample in a series of the JWST/NIRCam (and/or HST/WFC3 near-IR) bands.

We run `SExtractor` (Bertin & Arnouts 1996) to perform photometry in the JWST/NIRCam multiband images. The aperture has a radius of triple FWHMs of the point-spread function (PSF) in each wavelength band. The aperture correction is calculated from the PSF in each band. We first obtain initial measurements by matching the output catalogs to the targets within a distance tolerance of an FWHM. For each target, we select its brightest band to feed the detection image. Specifically, we adopt the F444W band for three sources covered by the PRIMER survey and the F460W band for the four sources covered by the UDF-MB survey because their Hα lines boost these bands. We then rerun `SExtractor` in the dual image mode with the detection images. For each measurement image, we also adopt an aperture with a radius of triple PSF FWHMs in this band. Only for the SC-7 source, we use a radius of 1.5 PSF FWHM, in order to minimize the amount of abnormal pixels within the photometric aperture, caused by the fact that SC-7 is located very close to the image edge. Table 1 lists the multiband photometry results of the galaxy sample.

3. Results

In this section, we give the measured results of UV and Hα quantities of the galaxy sample. Their UV properties are derived from JWST/NIRCam SW bands and/or HST/WFC3 near-IR bands. We utilize the NIRCam medium bands to constrain their (rest-frame) optical continua. We then measure their Hα flux by combining the corresponding LW broad or medium bands. We further obtain their Hα-related properties including the Lyα escape fraction and the ionizing photon production efficiency. The results are listed in Table 2.

3.1. UV Continua

We measure UV continua of the galaxies with the commonly used method (e.g., Pentericci et al. 2018; Jiang et al. 2020). As in these works, we assume a power-law form for the UV continuum of each source, i.e., $f_\lambda \propto \lambda^\beta$. As we work in AB magnitude units, we fit a linear relation $m_{AB} \propto (\beta + 2) \times \log(\lambda)$ to the SW photometric data from which we obtain the

---

[4] https://archive.stsci.edu/hlsp/candels

[5] https://github.com/spacetelescope/jwst

[6] https://github.com/gbrammer/grizli

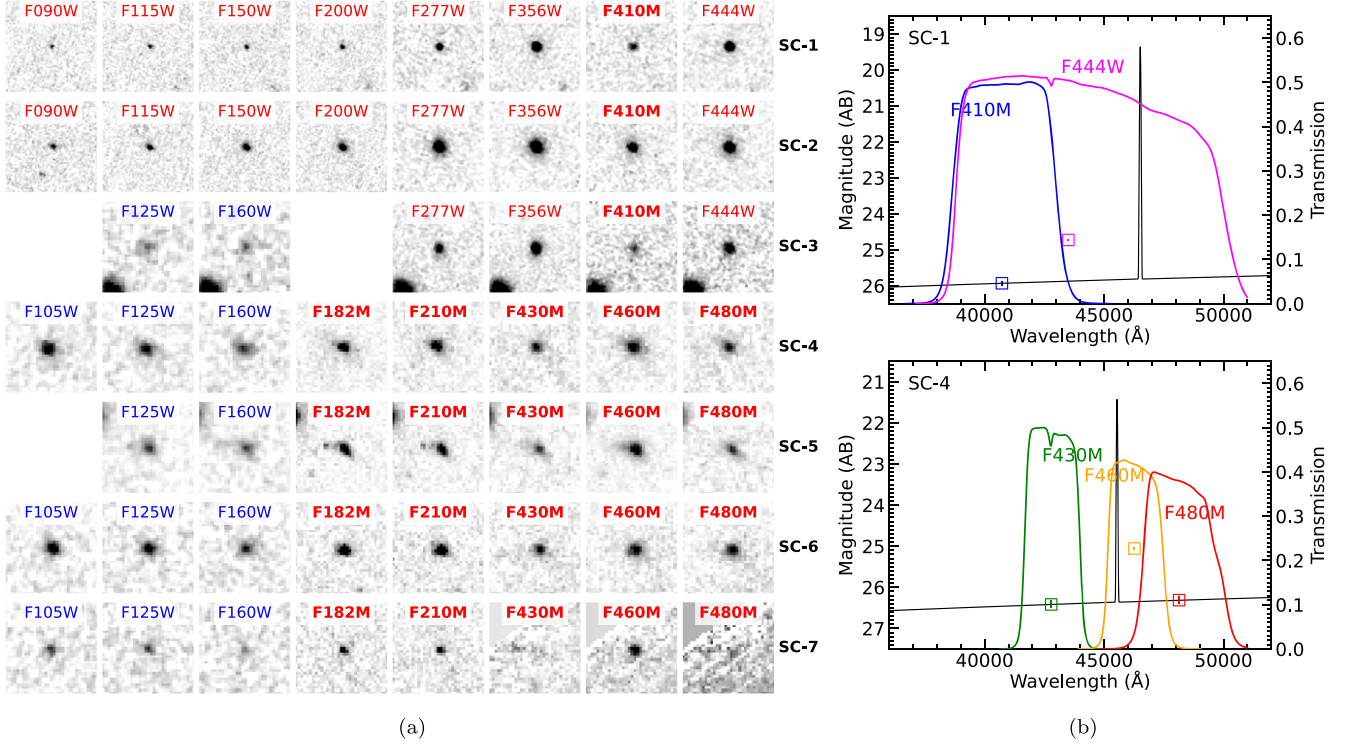[7] https://drizzlepac.readthedocs.io/en/latest/astrodrizzle.html

Figure 2. (a) Thumbnail images of the Lyα galaxies at $z \simeq 6$ in this work. Their ID names are marked at the right end of each row. The size of the images is $2'' \times 2''$ (north is up and east to the left). The corresponding band is marked at the top of each thumbnail image (HST/WFC3 bands in blue and JWST/NIRCam bands in red). The medium bands are shown in bold face. (b) Illustration of the measurement of the Hα+[N II] line flux of the seven sources (shown in the left figure) including three sources covered by the PRIMER survey (the upper panel gives an example) and four sources covered by the UDF-MB survey (the lower panel gives an example). The boxes with error bars are the photometry in the NIRCam LW bands. They have the same colors as the transmission curves of the five NIRCam filters. The black lines represent the power-law optical continua and Gaussian profiles (FWHM = 300 km s^{-1}) of Hα lines that boost the corresponding bands.

UV-continuum slope $\beta_{\rm UV}$ and the absolute UV magnitude $M_{\rm UV}$ at the rest-frame wavelength 1500 Å.

For a galaxy at $z \simeq 6$, its observed Lyα line is located in the wavelength range of the Subaru/z' and JWST/F090W bands. The corresponding broadband flux usually differs from the flux level of the UV continuum due to the Lyα emission or break (IGM absorption bluewards of Lyα). So, in the measurements for UV continua, we abandon the F090W photometric data for SC-1 and SC-2. We then subtract the fit power-law UV continuum from the z'- or F090W-band photometry to constrain Lyα flux and $\rm EW_0\,(Ly\alpha)$ for SC-1. The IGM continuum absorption blueward of the Lyα line is considered in the computation (Madau 1995). For SC-3–7, the CANDELz7 galaxies, we directly adopt the observed Lyα flux given by P18 to compute the Lyα luminosity and $\rm EW_0\,(Ly\alpha)$ with our obtained power-law UV continua. For SC-2, which is undetected in Lyα, we use the upper limit of $\rm EW_0\,(Ly\alpha)$ given by P18 to compute its Lyα flux. Note that the Lyα flux may be slightly underestimated due to the potential Lyα emission from the circumgalactic medium (e.g., Cai et al. 2019; Wu et al. 2020).

3.2. Hα Line Emission

We combine the medium and broad bands (covering the rest-frame optical wavelength at $z \simeq 6$) to estimate the flux and EW of Hα emission lines. In Figure 2, the (red) colors of F410M − F444W and F430M − F460M clearly show the flux excess due to strong Hα lines. In the F444W broad band, which covers the F410M, F430M, F460M, and F480M medium bands, Hα+[N II] lines dominate the flux estimation

(e.g., Anders & Fritze-v. Alvensleben 2003). We thus ignore other optical lines except for Hα+[N II]. We assume that [N II] contributes line flux at the Hα wavelength due to the small wavelength difference relative to the wavelength range of $>4\,\mu$m. We also assume that the emission line has a Gaussian profile with FWHM = 300 km s^{-1} (see the black lines in Figure 2(b)).

SC-4–7 are covered by the UDF-MB survey with five NIRCam medium bands. For SC-4, 5, and 7, we use the F430M and F480M magnitudes (3σ upper limit for SC-7) to constrain the rest-frame optical continuum with a power-law form $f_\nu \propto \nu^\alpha$ because the Hα+[N II] emission only falls into the F460M band. For SC-6, the Hα+[N II] emission falls into the F460M and F480M bands. We thus match the continuum plus line model to the three LW medium-band photometric data. Figure 2(b) illustrates the above procedure in the lower panel. For these four sources, we obtain similar power-law indices with a median value of $\alpha \sim -0.6$. SC-1–3 are covered by the PRIMER NIRCam multiband (7 broad + 1 medium) observations. As no strong nebular lines fall into the F410M band, we use the F410M magnitude to constrain the (rest-frame) optical continuum and the F410M − F444W color to estimate the Hα + [N II] flux. We start with a power-law continuum with an index of $\alpha_0 = -0.6$ (from the other four sources) to match the F410M flux density. Then, we integrate the known continuum plus unknown line emission weighted by the F444W filter transmission curve to match the F444M flux density and compute the Hα+[N II] flux. We also vary the continuum slope α in a reasonable range of $\alpha_0 \pm 0.5$ to obtain the deviations of the measured line flux, which would be

Table 2
Measured Properties of the Lyα Galaxy Sample at $z \simeq 6$

ID	$z_{Ly\alpha}$	β_{UV}	M_{UV}	$\log_{10} L(Ly\alpha)$ (erg s^{-1})	EW$_0$ (Lyα) (Å)	f_{esc}(Lyα)	$\log_{10} L(H\alpha)$ (erg s^{-1})	EW$_0$ (Hα) (Å)	$\log_{10} \xi_{ion,0}$ (Hz erg^{-1})	SFR(Hα) ($M_\odot$ yr^{-1})
(1)	(2)	(3)	(4)	(5)	(6)	(7)	(8)	(9)	(10)	(11)
SC-1	6.087	−2.03	−20.11	43.16	147	0.066 ± 0.014	43.27 ± 0.09	2756 ± 596	26.45 ± 0.19	100 ± 22
SC-2	5.810	−1.46	−21.06	<41.92	<4	<0.03	42.35 ± 0.16	113 ± 40	25.15 ± 0.31	12 ± 4
SC-3	6.297	−2.53	−20.46	42.54	23	0.055 ± 0.011	42.72 ± 0.09	994 ± 204	25.77 ± 0.18	28 ± 6
SC-4	5.939	−1.73	−20.51	42.44	20	0.088 ± 0.013	42.42 ± 0.06	663 ± 94	25.45 ± 0.12	14 ± 2
SC-5	5.938	−1.88	−20.93	42.15	7	0.027 ± 0.004	42.64 ± 0.06	767 ± 102	25.49 ± 0.12	23 ± 3
SC-6	6.108	−2.00	−20.39	42.10	10	0.082 ± 0.013	42.11 ± 0.07	267 ± 42	25.18 ± 0.13	7 ± 1
SC-7	5.916	−3.01	−19.08	42.94	186	0.470 ± 0.085	42.20 ± 0.08	1261 ± 227	25.79 ± 0.16	8 ± 2

included in the errors of the final values. Figure 2(b) illustrates the above procedure in the upper panel.

After estimating the line flux, we assume that Hα accounts for 85% of the Hα+[N II] flux, which is similar to previous studies (e.g., Rasappu et al. 2016; Faisst et al. 2019; Sun et al. 2022). To be conservative, we also feed the 10% flux into the error of the final Hα flux. With the measured flux of the Hα line, we obtain the SFR(Hα) using the canonical Hα–SFR calibration relation (listed in Column 11 of Table 2; Hao et al. 2011; Murphy et al. 2011; Kennicutt & Evans 2012). We further compute the EW$_0$ (Hα) with the rest-frame optical continuum level. The results are plotted in the second and third rows of Figure 3. Note that the Hα flux and EW may be underestimated because the optical continuum is overestimated due to the existence of some faint optical lines. But such an underestimation is supposed to be included in the enlarged measurement errors. EW$_0$ (Hα) indicates the specific SFR (sSFR) of galaxies. Our $z \simeq 6$ sample has a larger range of EW$_0$ (Hα) than the low-z LAEs (Matthee et al. 2021) and local analogs (Yang et al. 2017). Recently, Sun et al. (2022) serendipitously found a sample of strong Hα/[O III] emitters in the JWST/NIRCam wide-field slitless spectroscopy (WFSS) data. Our median EW$_0$ (Hα) is twice higher than theirs because in our sample, the six of the seven galaxies emitting Lyα lines are supposed to have higher sSFR while the SF galaxies of Sun et al. (2022) are found based on Hα/[O III] detections. SC-7 is undetected in Lyα and its EW$_0$ (Hα) is similar to the lowest one of the sample in Sun et al. (2022).

3.3. Hα-related Properties

3.3.1. Escape Fraction of Lyα Photons

We estimate the escape fraction of Lyα photons ($f_{esc}^{Ly\alpha}$) for the sample. With the obtained Hα flux, we adopt the canonical ratio $L(Ly\alpha)/L(H\alpha) = 8.7$ (e.g., Henry et al. 2015) to calculate the intrinsic Lyα flux and obtain

$$f_{esc}^{Ly\alpha} = \frac{L_{obs}(Ly\alpha)}{L(H\alpha) \times 8.7} \quad (1)$$

under the assumption of Case B recombination in $T_e = 10^4 K$ (Osterbrock & Ferland 2006). We also apply a dust correction using the reddening law of Calzetti et al. (2000). We cannot well constrain the extinction $E(B - V)$ for nebulae due to the lack of Balmer decrement (Hα/Hβ) information. Thus, we perform SED fitting using BAGPIPES (Carnall et al. 2018) and obtain $A_V = 0.8$ for SC-2 thanks to the abundance of multiband photometric data for this source. For others, we adopt a lower and modest value of

$A_V = 0.4$ as a reasonable assumption because they have higher EW$_0$ (Lyα) with lower dust content. Note that A_V is supposed to be smaller for the six galaxies but the difference is only $\lesssim 0.1$ dex for the computed $f_{esc}^{Ly\alpha}$. The $f_{esc}^{Ly\alpha}$ results are listed in Column 7 of Table 2. We can see that six of the seven galaxies have $f_{esc}^{Ly\alpha} \lesssim 10\%$ even though they are spread over a large range of EW$_0$ (Lyα) and EW$_0$ (Hα). This may imply the upper limit of $f_{esc}^{Ly\alpha}$ for most galaxies at $z \simeq 6$. Note that f_{esc}^{LyC} is supposed to be smaller than the $f_{esc}^{Ly\alpha}$ (e.g., Dijkstra et al. 2016; Izotov et al. 2020). SC-7 has the largest value of $f_{esc}^{Ly\alpha}$ reaching $\simeq 50\%$ while it is relatively faint in the rest-frame UV ($M_{UV} \simeq -19$) with an extremely blue UV slope ($\beta_{UV} \simeq -3$). In Section 4.1, we discuss the relevant, potential trends.

3.3.2. Production Efficiency of Ionizing Photons

With the measured flux of UV continua and Hα line, we estimate the hydrogen-ionizing photon production efficiency ξ_{ion} by

$$\xi_{ion} = \frac{\dot{N}_{ion}}{L_\nu^{UV}}, \quad (2)$$

where $\dot{N}_{ion}$ (s^{-1}) is the intrinsic production rate of hydrogen-ionizing photons from stellar populations and L_ν^{UV} (erg s^{-1} Hz^{-1}) is the (monochromatic) UV-continuum luminosity per photon frequency that can be derived from the above-measured M_{UV}. ξ_{ion} intrinsically depends on the assumed stellar population model (e.g., Robertson et al. 2013; Eldridge et al. 2017; Yung et al. 2020b). $\dot{N}_{ion}$ can be computed from Hα emission by

$$\dot{N}_{ion} = \frac{L(H\alpha)}{1 - f_{esc}^{LyC}} \times 7.35 \times 10^{11} \, erg^{-1} \quad (3)$$

in the ($T_e = 10^4 K$) Case B recombination (Kennicutt et al. 1994; Leitherer & Heckman 1995; Madau et al. 1998). We then obtain the production efficiency of ionizing photons that do not escape from the galaxy, $\xi_{ion,0}$ assuming $f_{esc}^{LyC} = 0$.

The (dust-uncorrected) results are shown in the last row of Figure 3. Note that the dust-corrected values are lower by $\lesssim 0.1$ dex assuming the canonical stellar/nebular extinction ratio of 0.44, which is obtained from local starbursts (Calzetti et al. 2000). The $\xi_{ion,0}$ results are listed in Column 10 of Table 2. Our obtained $\xi_{ion,0}$ are distributed over a broad range of $\log_{10} \xi_{ion,0} \sim 25.0–26.5$. The median value is consistent with that of a large UV-faint galaxy sample from Prieto-Lyon et al. (2022). This median is also close to that of a Hα-emitter sample
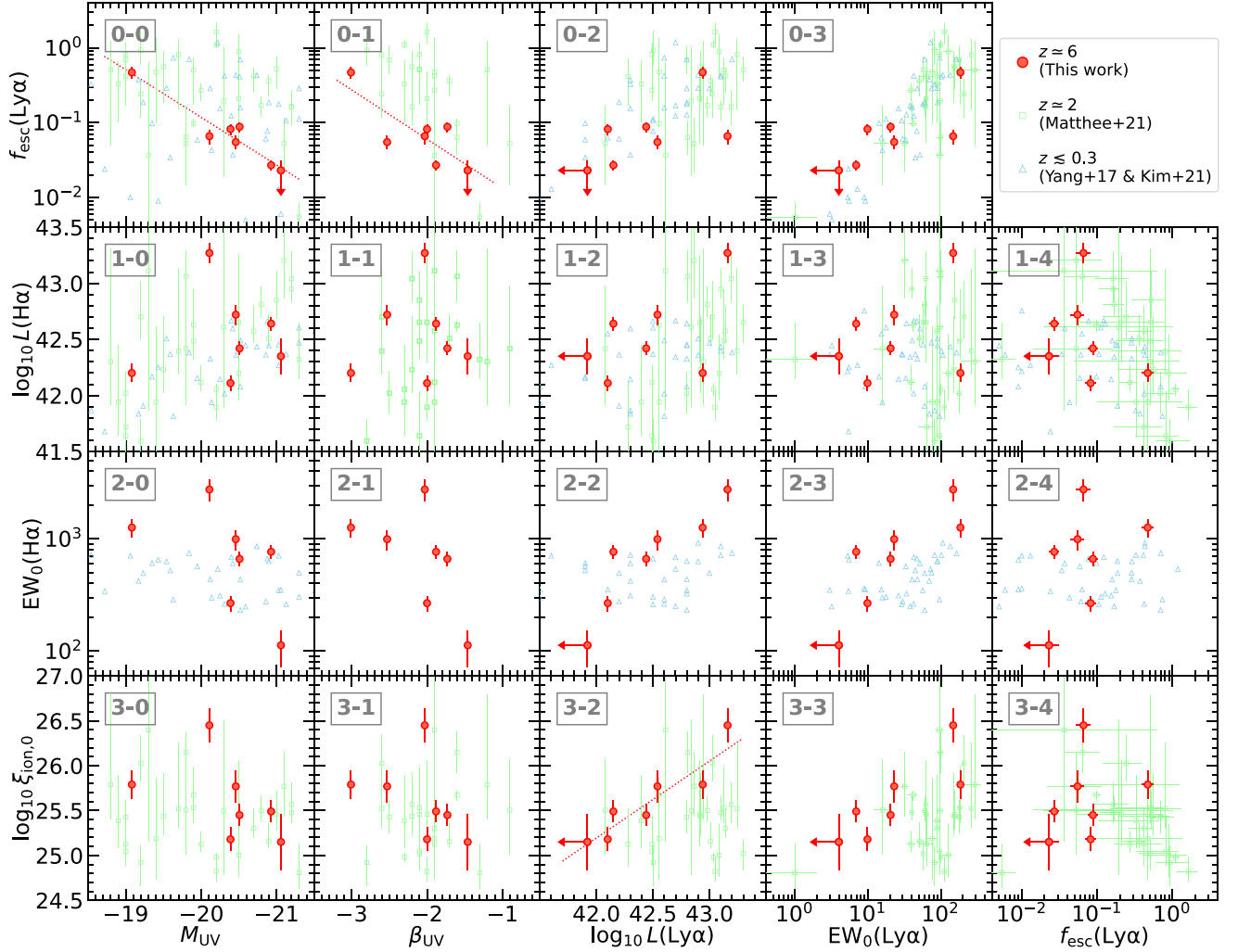
Figure 3. Comparison of the measured Hα-related properties with the Lyα and UV properties. From top to bottom, we show the Lyα escape fraction, Hα luminosity, rest-frame Hα EW, and ionizing photon production efficiency. From left to right, we show the rest-frame UV magnitude, UV slope, Lyα luminosity, and rest-frame Lyα EW. We also compare the Lyα escape fraction with the measured Hα properties in the rightmost column. The red circles indicate the $z \simeq 6$ galaxies measured by this work. The green squares represent the $z \sim 2$ LAEs from Matthee et al. (2021). The blue triangles correspond to the local Green Pea galaxies from Yang et al. (2017) and Kim et al. (2021). The red dotted lines indicate the best linear fits to the measured quantities (red circles).

from Sun et al. (2022). Among our sample, SC-1 is the most luminous in Lyα and has the highest $\xi_{\rm ion,0}$ reaching $\log_{10} \xi_{\rm ion,0} \sim 26.5$ while SC-2 is not detected in Lyα and has the lowest $\xi_{\rm ion,0}$. We further give an extensive discussion in the next section.

4. Discussion

Thanks to the excellent capability of JWST (Rigby et al. 2022), we have measured the Hα-related properties of the SF galaxies at $z \simeq 6$. In this section, we discuss the obtained properties of the galaxy sample. We compare our results with previous studies in Figure 3. The Hα-related properties are assigned by rows and Lyα/UV quantities are assigned by columns. The $f_{\rm esc}^{\rm Ly\alpha}$ is assigned again at the rightmost column to compare with the Hα-related properties.

4.1. $f_{\rm esc}^{\rm Ly\alpha}$–UV Correlation

We compare the obtained $f_{\rm esc}^{\rm Ly\alpha}$ in the top row and rightmost column of Figure 3. The measured results show that $f_{\rm esc}^{\rm Ly\alpha}$

positively correlates with $L({\rm Ly\alpha})$ and $EW_0({\rm Ly\alpha})$, and negatively correlates with $M_{\rm UV}$ and $\beta_{\rm UV}$ (in the top row). The positive trends are natural because $f_{\rm esc}^{\rm Ly\alpha}$ is inferred from the Lyα flux, which is similar to those found from the low-z samples (e.g., Hayes et al. 2014; Yang et al. 2017; Matthee et al. 2021). Yang et al. (2017) (and Kim et al. 2021) use a statistical sample of local Green Pea galaxies as high-z analogs to reveal that. Matthee et al. (2021) use an LAE sample at $z \sim 2$ and also found such a relation. For the negative trends of $f_{\rm esc}^{\rm Ly\alpha}$ changing as UV properties, we obtain a linear relation between $f_{\rm esc}^{\rm Ly\alpha}$ and $M_{\rm UV}$,

$$\log_{10} f_{\rm esc}^{\rm Ly\alpha} = (0.64 \pm 0.08) M_{\rm UV} + (11.8 \pm 1.7), \quad (4)$$

shown as a red dotted line in panel 0–0; we also obtain another linear relation between $f_{\rm esc}^{\rm Ly\alpha}$ and $\beta_{\rm UV}$,

$$\log_{10} f_{\rm esc}^{\rm Ly\alpha} = (-0.66 \pm 0.23) \beta_{\rm UV} - (2.5 \pm 0.5), \quad (5)$$

shown as a red dotted line in panel 0–1. The $f_{\rm esc}^{\rm Ly\alpha}$–$M_{\rm UV}$ relation seems to exist in the current high-z sample, although the sign is weak for the two samples of Lyα galaxies at lower redshifts.
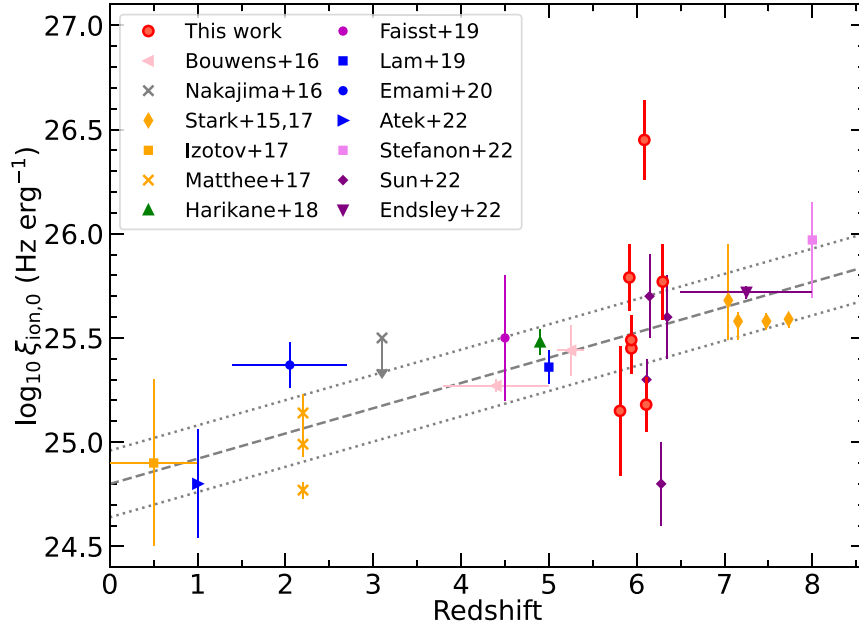
Figure 4. Redshift evolution of $\xi_{ion,0}$ for SF galaxies. The red circle symbols mark our results. Other symbols represent the literature studies including Bouwens et al. (2016), Nakajima et al. (2016), Stark et al. (2015), Stark et al. (2017), Izotov et al. (2017), Matthee et al. (2017a), Harikane et al. (2018), Faisst et al. (2019), Lam et al. (2019), Emami et al. (2020), Atek et al. (2022), Stefanon et al. (2022), Sun et al. (2022), and Endsley et al. (2022). The gray dashed line indicates the best-fit linear relation with a 1σ uncertainty region enclosed by the gray dotted lines.

Chisholm et al. (2022) found that f_{esc}^{LyC} increases for fainter M_{UV} using a sample of LyC-leaking SF galaxies at $z \simeq 0.3$, which is overall lower than our obtained $f_{esc}^{Ly\alpha}$–M_{UV} trend. Such difference is consistent with the scenario of $f_{esc}^{LyC} \lesssim f_{esc}^{Ly\alpha}$ (e.g., de Barros et al. 2016; Dijkstra et al. 2016).

The $f_{esc}^{Ly\alpha}$–β_{UV} trend may exist at $z \simeq 6$ like at $z \sim 2$ (e.g., Prieto-Lyon et al. 2022; Snapp-Kolas et al. 2022). The reason can be simply interpreted as bluer galaxies having a younger stellar population and/or lower dust content. They emit harder ionizing photons suffering lower extinction, which accounts for the higher escape fraction of Lyα photons. The $z \simeq 6$ trend is steeper, which is consistent with the current consensus that galaxies at higher redshift are bluer (e.g., Bouwens et al. 2014; Jiang et al. 2020). Chisholm et al. (2022) show that f_{esc}^{LyC} scales strongly with β_{UV} for the LyC-leaker sample at $z \simeq 0.3$, while those with $\beta_{UV} = -2$ have an averaged $f_{esc}^{LyC} \lesssim 5\%$, which is smaller than $f_{esc}^{Ly\alpha} \lesssim 10\%$ estimated from our linear fit (panel 0–1 of Figure 3). SC-7 is the bluest one in our sample with $f_{esc}^{Ly\alpha} \sim 50\%$. This galaxy and the luminous LAEs with very blue UV continua ($\beta_{UV} \lesssim 3$) reported by Jiang et al. (2020) are supposed to be strong LyC leakers to contribute ionizing photons. They are thus excellent targets to carry out JWST IR spectroscopic follow-up observations for the ionization lines.

4.2. $\xi_{ion,0}$–Lyα Correlation

Panel 3–2 (3–3) of Figure 3 shows a potential correlation between the $\xi_{ion,0}$ and Lyα luminosity (or Lyα equivalent width) for the $z \simeq 6$ sample in this work. We obtain a linear relation between $\xi_{ion,0}$ and $L(Ly\alpha)$:

$$\log_{10} \xi_{ion,0} = (0.87 \pm 0.19)\log_{10} L(Ly\alpha) - (11.3 \pm 8.2),$$

(6)

shown as a red dotted line in panel 3–2. Saldana-Lopez et al. (2022) also found a similar trend in a sample of SF galaxies at $3 \leqslant z \leqslant 5$. We notice that such correlations are not always retained for the LAEs at $z \sim 2$ from Matthee et al. (2021), especially for those with a relatively bright Lyα flux. A direct reason is that the $z \sim 2$ LAEs in Matthee et al. (2021) generally have higher $f_{esc}^{Ly\alpha}$, even reaching $\gtrsim 1$. Matthee et al. (2017b) also obtained that several galaxies have $f_{esc}^{Ly\alpha} \gtrsim 1$, and they explained it using mechanisms including, for example, Lyα emission being produced by a different mechanism (like cooling radiation; Dijkstra 2014). We look forward to comparing their results updated with the additional Hα information.

The $\xi_{ion,0}$–$L(Ly\alpha)$ trend can be reasonably expected because the harder ionizing radiation of more young stellar populations (higher sSFR shown by the panel 2–2) tend to produce more ionizing photons per non-ionizing photons (e.g., Balestra et al. 2013; Mainali et al. 2017) and ionize the ISM more efficiently, eventually enhancing Lyα production, transfer, and escape. Note that $EW_0(Ly\alpha)$ can be inferred to be proportional to $\xi_{ion} \times f_{esc}^{Ly\alpha}$ (e.g., Harikane et al. 2018). This trend implies that galaxies with $\log_{10} L(Ly\alpha) \gtrsim 43.5$ (at the bright end of the Lyα luminosity function) may have a high ionizing photon production efficiency reaching $\log_{10} \xi_{ion,0} \gtrsim 27$. Conversely speaking, SF galaxies with low $\xi_{ion,0}$ ($\lesssim 25$) may tend to emit negligible Lyα emission. If such a trend exists, the very (Lyα) luminous galaxies could fully ionize their surrounding neutral H I gas with a modest or even a small f_{esc}^{LyC} value. This situation is also consistent with the scenario that luminous Lyα galaxies in the EoR power large ionizing bubbles (e.g., Zheng et al. 2017; Yajima et al. 2018; Hu et al. 2021; Ning et al. 2022).

4.3. Implications of High ξ_{ion}

We plot the redshift evolution of $\xi_{ion,0}$ for the SF galaxies in Figure 4. The red circle symbols indicate our results for the Lyα galaxies at the end of EoR. The figure shows that the $\xi_{ion,0}$ of SF galaxies increases with redshift. Among the seven Lyα galaxies, three of them (SC-1, 3, and 7) have high production efficiency of ionizing photons of $\log_{10} \xi_{ion,0} \gtrsim 26$. This fact reveals the possibility that a portion of galaxies has high values of ξ_{ion}. Maseda et al. (2020) also found an elevated mean ξ_{ion} ($\log_{10} \xi_{ion} \gtrsim 26$) in a sample of UV-faint and high-EW LAEs at $z \approx 4$–5. Finkelstein et al. (2019) presented a reionization model dominated by low-mass and UV-faint galaxies, which would require such high ξ_{ion}. Our results provide observational evidence. The high values of ξ_{ion} have not been well explained in galaxy simulations. For example, Wilkins et al. (2016) explored the ξ_{ion} range of EoR galaxies in the BlueTides simulation, in which they used low-metallicity stellar population (with binary systems) models to obtain their highest ξ_{ion} of $\log_{10} \xi_{ion} \lesssim 26$. Yung et al. (2020b) could not also provide such high ξ_{ion} with the semianalytical models of galaxy formation. Note that their models only predict a rather weak dependence of ξ_{ion} with redshift, which means we have not understood well the physical processes responsible for the redshift evolution shown in Figure 4 (the gray lines). Meanwhile, a larger sample of fainter galaxies is necessary to be built to overcome the sampling bias at the higher redshift ($z > 5$).

The median $\xi_{ion,0}$ of our Lyα galaxy sample is consistent with the overall trend (gray lines). Previous results indicate that EoR SF galaxies with $\xi_{ion,0}$ on the overall trend can provide enough ionizing photon budget (e.g., Harikane et al. 2018; Stefanon et al. 2022). Our sample implies that Lyα galaxies may also play a similar role and contribute to the total balance of ionizing photons at $z \simeq 6$. Note that the most luminous Lyα galaxy in the sample, SC-1 (identified by our Magellan M2FS survey), has a very high $\xi_{ion,0}$ ($\log_{10} \xi_{ion,0} \sim 26.5$) relative to other SF galaxies even though its Lyα luminosity of $\log_{10} L(Ly\alpha) \simeq 43$ is only a little larger than the characteristic luminosity of Lyα luminosity function (e.g., Hu et al. 2010; Kashikawa et al. 2011; Zheng et al. 2017; Ning et al. 2022). Its nature needs to be revealed using further spectroscopic observations. Our results support that Lyα galaxies, especially those with intrinsically high $EW_0(Ly\alpha)$, may significantly contribute ionizing photons during the EoR. We look forward to comparing our findings with the ionizing photon production efficiency estimated for other Lyα-luminous galaxies (from, e.g., Ning et al. 2020, 2022), which will be partially covered by the JWST observations.

5. Summary

In this work, we present a pilot study of a spectroscopically confirmed sample of (Lyα-emitting) galaxies at redshift $z \simeq 6$ based on the JWST/NIRCam imaging data. The sample includes seven targets: one identified by our Magellan/M2FS spectroscopic survey and six observed by the previous CANDELSz7 survey. All seven sources we analyze are Lyman-break galaxies showing large differences in their Lyα luminosity, ranging from no observed Lyα line up to a strong Lyα line of $\log_{10} L(Ly\alpha) \simeq 43.3$. These objects have been covered by two JWST/NIRCam imaging surveys, PRIMER and UDF-MB, which employ a series of SW and LW bands.

We have obtained their Lyα- and Hα-related properties by combining the NIRCam broad and/or medium bands. Based on the results, we also revealed the potential correlations among the properties of Lyα galaxies at $z \simeq 6$. We summarize our findings as follows:

1. Six of seven galaxies have Lyα escape fractions of $f_{esc}^{Ly\alpha} \lesssim 10\%$ regardless of their $EW_0(Ly\alpha)$ and $EW_0(H\alpha)$, which might be the status for most of the star-forming galaxies at $z \simeq 6$.
2. One Lyα galaxy, which is relatively faint in the rest-frame UV ($M_{UV} \simeq -19$) with an extremely blue UV slope ($\beta_{UV} \simeq -3$), has a Lyα escape fraction reaching $f_{esc}^{Ly\alpha} \simeq 50\%$.
3. Lyα galaxies with fainter rest-frame UV continua and/or bluer UV slopes tend to have higher escape fractions of Lyα photons (Equations (4) and (5)).
4. Our sample is spread over a broad range of the ionizing photon production efficiency over $\log_{10} \xi_{ion,0} \sim 25.0$–26.5 with a median value close to those of the galaxy samples at similar redshifts from other studies.
5. Galaxies with more luminous Lyα emission probably have higher production efficiencies of ionizing photons (Equation (6)).
6. Our identified source (SC-1 analyzed in this study), which is very luminous in Lyα, has a very high ionizing photon production efficiency of $\log_{10} \xi_{ion,0}$ (Hz erg^{-1}) > 26. Its nature merits further investigation.

Our results agree with the scenario in which Lyα galaxies may serve as a significant contributor to cosmic reionization. The bluer and/or more luminous Lyα galaxies are ideal targets for JWST spectroscopic follow-up observations. We need a larger sample of Lyα galaxies observed by JWST for further analysis on the reionization sources.

ORCID iDs

Yuanhang Ning ⬤ https://orcid.org/0000-0001-9442-1217
Zheng Cai ⬤ https://orcid.org/0000-0001-8467-6478
Linhua Jiang ⬤ https://orcid.org/0000-0003-4176-6486
Xiaojing Lin ⬤ https://orcid.org/0000-0001-6052-4234
Shuqi Fu ⬤ https://orcid.org/0000-0003-0964-7188
Daniele Spinoso ⬤ https://orcid.org/0000-0002-9074-4833

References

Anders, P., & Fritze-v. Alvensleben, U. 2003, A&A, 401, 1063

Arrabal Haro, P., Rodríguez Espinosa, J. M., Muñoz-Tuñón, C., et al. 2020, MNRAS, 495, 1807

Atek, H., Furtak, L. J., Oesch, P., et al. 2022, MNRAS, 511, 4464

Balestra, I., Vanzella, E., Rosati, P., et al. 2013, A&A, 559, L9

Bertin, E., & Arnouts, S. 1996, A&AS, 117, 393

Bouwens, R. J., Illingworth, G. D., Oesch, P. A., et al. 2014, ApJ, 793, 115

Bouwens, R. J., Smit, R., Labbé, I., et al. 2016, ApJ, 831, 176

Cai, Z., Cantalupo, S., Prochaska, J. X., et al. 2019, ApJS, 245, 23

Calzetti, D., Armus, L., Bohlin, R. C., et al. 2000, ApJ, 533, 682

Carnall, A. C., McLure, R. J., Dunlop, J. S., & Davé, R. 2018, MNRAS, 480, 4379

Casey, C. M., Kartaltepe, J. S., Drakos, N. E., et al. 2022, arXiv:2211.07865

Chisholm, J., Saldana-Lopez, A., Flury, S., et al. 2022, MNRAS, 517, 5104

Dayal, P., & Ferrara, A. 2012, MNRAS, 421, 2568

de Barros, S., Vanzella, E., Amorín, R., et al. 2016, A&A, 585, A51

de La Vieuville, G., Pelló, R., Richard, J., et al. 2020, A&A, 644, A39

Dijkstra, M. 2014, PASA, 31, e040

Dijkstra, M., Gronke, M., & Venkatesan, A. 2016, ApJ, 828, 71

Dunlop, J. S., Abraham, R. G., Ashby, M. L. N., et al. 2021, PRIMER: Public Release IMaging for Extragalactic Research, JWST Proposal, 1837

Eldridge, J. J., Stanway, E. R., Xiao, L., et al. 2017, PASA, 34, e058

Emami, N., Siana, B., Alavi, A., et al. 2020, ApJ, 895, 116

Endsley, R., Stark, D. P., Whitler, L., et al. 2022, arXiv:2208.14999

Faisst, A. L., Capak, P., Hsieh, B. C., et al. 2016, ApJ, 821, 122

Faisst, A. L., Capak, P. L., Emami, N., Tacchella, S., & Larson, K. L. 2019, ApJ, 884, 133

Finkelstein, S. L., D'Aloisio, A., Paardekooper, J.-P., et al. 2019, ApJ, 879, 36

Flury, S. R., Jaskot, A. E., Ferguson, H. C., et al. 2022, ApJ, 930, 126

Galametz, A., Grazian, A., Fontana, A., et al. 2013, ApJS, 206, 10

Gardner, J. P., Mather, J. C., Clampin, M., et al. 2006, SSRv, 123, 485

Grogin, N. A., Kocevski, D. D., Faber, S. M., et al. 2011, ApJS, 197, 35

Guo, Y., Ferguson, H. C., Giavalisco, M., et al. 2013, ApJS, 207, 24

Hao, C.-N., Huang, J.-S., Xia, X., et al. 2018, ApJ, 864, 145

Hao, C.-N., Kennicutt, R. C., Johnson, B. D., et al. 2011, ApJ, 741, 124

Harikane, Y., Ouchi, M., Shibuya, T., et al. 2018, ApJ, 859, 84

Hayes, M., Östlin, G., Duval, F., et al. 2014, ApJ, 782, 6

Henry, A., Scarlata, C., Martin, C. L., & Erb, D. 2015, ApJ, 809, 19

Hu, E. M., Cowie, L. L., Barger, A. J., et al. 2010, ApJ, 725, 394

Hu, W., Wang, J., Infante, L., et al. 2021, NatAs, 5, 485

Inami, H., Bacon, R., Brinchmann, J., et al. 2017, A&A, 608, A2

Izotov, Y. I., Guseva, N. G., Fricke, K. J., Henkel, C., & Schaerer, D. 2017, MNRAS, 467, 4118

Izotov, Y. I., Schaerer, D., Thuan, T. X., et al. 2016, MNRAS, 461, 3683

Izotov, Y. I., Schaerer, D., Worseck, G., et al. 2020, MNRAS, 491, 468

Jiang, L., Cohen, S. H., Windhorst, R. A., et al. 2020, ApJ, 889, 90

Jiang, L., Finlator, K., Cohen, S. H., et al. 2016, ApJ, 816, 16

Jiang, L., Ning, Y., Fan, X., et al. 2022, NatAs, 6, 850

Jiang, L., Shen, Y., Bian, F., et al. 2017, ApJ, 846, 134

Jones, T., Stark, D. P., & Ellis, R. S. 2012, ApJ, 751, 51

Kartaltepe, J., Casey, C. M., Bagley, M., et al. 2021, COSMOS-Webb: The Webb Cosmic Origins Survey, JWST Proposal, 1727

Kashikawa, N., Shimasaku, K., Malkan, M. A., et al. 2006, ApJ, 648, 7

Kashikawa, N., Shimasaku, K., Matsuda, Y., et al. 2011, ApJ, 734, 119

Kennicutt, R. C., & Evans, N. J. 2012, ARA&A, 50, 531

Kennicutt, R. C., Jr., Tamblyn, P., & Congdon, C. E. 1994, ApJ, 435, 22

Kim, K. J., Malhotra, S., Rhoads, J. E., & Yang, H. 2021, ApJ, 914, 2

Koekemoer, A. M., Faber, S. M., Ferguson, H. C., et al. 2011, ApJS, 197, 36

Lam, D., Bouwens, R. J., Labbé, I., et al. 2019, A&A, 627, A164

Leitherer, C., & Heckman, T. M. 1995, ApJS, 96, 9

Leitherer, C., Hernandez, S., Lee, J. C., & Oey, M. S. 2016, ApJ, 823, 64

Madau, P. 1995, ApJ, 441, 18

Madau, P., Pozzetti, L., & Dickinson, M. 1998, ApJ, 498, 106

Mainali, R., Kollmeier, J. A., Stark, D. P., et al. 2017, ApJL, 836, L14

Maseda, M. V., Bacon, R., Lam, D., et al. 2020, MNRAS, 493, 5120

Mateo, M., Bailey, J. I., Crane, J., et al. 2012, Proc. SPIE, 8446, 84464Y

Matthee, J., Sobral, D., Best, P., et al. 2017a, MNRAS, 465, 3637

Matthee, J., Sobral, D., Darvish, B., et al. 2017b, MNRAS, 472, 772

Matthee, J., Sobral, D., Hayes, M., et al. 2021, MNRAS, 505, 1382

Murphy, E. J., Condon, J. J., Schinnerer, E., et al. 2011, ApJ, 737, 67

Nakajima, K., Ellis, R. S., Iwata, I., et al. 2016, ApJL, 831, L9

Ning, Y., Jiang, L., Zheng, Z.-Y., et al. 2020, ApJ, 903, 4

Ning, Y., Jiang, L., Zheng, Z.-Y., & Wu, J. 2022, ApJ, 926, 230

Oke, J. B. 1974, ApJS, 27, 21

Osterbrock, D. E., & Ferland, G. J. 2006, Astrophysics of Gaseous Nebulae and Active Galactic Nuclei (Sausalito, CA: Univ. Science Books)

Pentericci, L., Vanzella, E., Castellano, M., et al. 2018, A&A, 619, A147

Prieto-Lyon, G., Strait, V., Mason, C. A., et al. 2022, arXiv:2211.12548

Rasappu, N., Smit, R., Labbé, I., et al. 2016, MNRAS, 461, 3886

Rigby, J., Perrin, M., McElwain, M., et al. 2022, arXiv:2207.05632

Robertson, B. E., Ellis, R. S., Furlanetto, S. R., & Dunlop, J. S. 2015, ApJL, 802, L19

Robertson, B. E., Furlanetto, S. R., Schneider, E., et al. 2013, ApJ, 768, 71

Saldana-Lopez, A., Schaerer, D., Chisholm, J., et al. 2022, arXiv:2211.01351

Santos, S., Sobral, D., Matthee, J., et al. 2020, MNRAS, 493, 141

Schaerer, D., & de Barros, S. 2009, A&A, 502, 423

Shapley, A. E., Steidel, C. C., Strom, A. L., et al. 2016, ApJL, 826, L24

Shibuya, T., Ouchi, M., Harikane, Y., et al. 2018, PASJ, 70, S15

Snapp-Kolas, C., Siana, B., Gburek, T., et al. 2022, arXiv:2211.00041

Stark, D. P., Ellis, R. S., Charlot, S., et al. 2017, MNRAS, 464, 469

Stark, D. P., Walth, G., Charlot, S., et al. 2015, MNRAS, 454, 1393

Stefanon, M., Bouwens, R. J., Illingworth, G. D., et al. 2022, ApJ, 935, 94

Stefanon, M., Labbé, I., Oesch, P. A., et al. 2021, ApJS, 257, 68

Steidel, C. C., Giavalisco, M., Dickinson, M., & Adelberger, K. L. 1996, AJ, 112, 352

Sun, F., Egami, E., Pirzkal, N., et al. 2022, arXiv:2209.03374

Taylor, A. J., Cowie, L. L., Barger, A. J., Hu, E. M., & Songaila, A. 2021, ApJ, 914, 79

Verhamme, A., Orlitová, I., Schaerer, D., et al. 2017, A&A, 597, A13

Verhamme, A., Orlitová, I., Schaerer, D., & Hayes, M. 2015, A&A, 578, A7

Wilkins, S. M., Feng, Y., Di-Matteo, T., et al. 2016, MNRAS, 458, L6

Williams, C. C., Maseda, M., Tacchella, S., et al. 2021, UDF Medium Band Survey: Using H-alpha Emission to Reconstruct Ly-alpha Escape during the Epoch of Reionization, JWST Proposal, 1963

Wu, J., Jiang, L., & Ning, Y. 2020, ApJ, 891, 105

Yajima, H., Sugimura, K., & Hasegawa, K. 2018, MNRAS, 477, 5406

Yang, H., Malhotra, S., Gronke, M., et al. 2017, ApJ, 844, 171

Yung, L. Y. A., Somerville, R. S., Finkelstein, S. L., et al. 2020a, MNRAS, 496, 4574

Yung, L. Y. A., Somerville, R. S., Popping, G., & Finkelstein, S. L. 2020b, MNRAS, 494, 1002

Zheng, Z.-Y., Wang, J., Rhoads, J., et al. 2017, ApJL, 842, L22